



Influence of plasma electrolytic oxidation on fatigue performance of AZ61 magnesium alloy [☆]



A. Němcová^a, P. Skeldon^{a,*}, G.E. Thompson^a, S. Morse^b, J. Čížek^c, B. Pacal^c

^aCorrosion and Protection Group, School of Materials, The University of Manchester, Manchester M13 9PL, UK

^bMaterial Science Centre, School of Materials, The University of Manchester, Manchester M13 9PL, UK

^cInstitute of Materials Science and Engineering, Faculty of Mechanical Engineering, Brno University of Technology, Technická 2, Brno, Czech Republic

ARTICLE INFO

Article history:

Received 22 November 2013

Accepted 27 December 2013

Available online 7 January 2014

Keywords:

A: Magnesium

B: SEM

C: Corrosion fatigue

C: Oxide coatings

ABSTRACT

The effect of plasma electrolytic oxidation (PEO) on the fatigue of AZ61 magnesium alloy has been investigated under high cycle conditions in air and 3.5% NaCl solution. PEO employed an alkaline pyrophosphate–silicate–fluoride electrolyte, with an offset square waveform, a frequency of 50 Hz, and current density of 130 mA cm⁻². The PEO treatment led to reductions in the fatigue limit by 38% in air and by 56% in 3.5% NaCl solution. The reduction of the fatigue limit is attributed to cracking of the coating, roughness of the alloy/coating interface, corrosion and influences of Al–Mn particles.

© 2014 The Authors. Published by Elsevier Ltd. Open access under [CC BY license](https://creativecommons.org/licenses/by/4.0/).

1. Introduction

Magnesium alloys are attractive for many applications because of their light weight compared with materials such as steels and aluminium alloys [1–3]. The alloys exhibit high specific strength, good castability and excellent shock resistance, and are also recyclable [4], but the corrosion resistance may be inadequate for some applications [1,5,6]. The corrosion resistance can be improved by reducing the concentrations of alloy impurities, especially iron, nickel and copper [7–9]. Protective treatments can also be applied, such as conversion coating, electroplating/electroless plating and anodizing [10]. Electrochemical processes are able to produce relatively thick, protective coatings [11], with much recent attention being given to plasma electrolytic oxidation (PEO) [12,13]. Ceramic coatings produced by PEO can provide high wear resistance and corrosion protection, the latter especially when the coating forms part of a paint scheme [13,14]. They are usually formed in aqueous electrolytes at high voltages, with the coating material being produced at locations of short-lived discharges [15]. Alkaline silicate or phosphate electrolytes, with various additives, such as borate [16] or fluoride [17], are often used. Fluoride ions may promote the formation of a protective barrier film [11,18], which can provide

resistance to pitting corrosion. They may also promote sparking [11] and increase the wear resistance of the coatings [19].

For some applications, retention of fatigue strength after surface treatment is critical. Studies of fatigue of electrochemically treated magnesium alloys have yielded variable results. It has been reported that the Anomag process caused no change in the fatigue properties of AZ91 alloy [20]. In contrast, 7 and 15 μm thick coatings produced by the Keronite process caused 3% and 10% reductions respectively in the fatigue limit of a Mg–2%Al–1%Zn–0.2%Mn alloy [21]. Khan et al. reported a 30% reduction due to an unspecified anodic layer on AM60 alloy [22]. The corrosion fatigue of magnesium alloys has not been extensively studied. Further, the many influencing factors, such as alloy composition, production route, corrosion environment and fatigue conditions, make it difficult to draw general conclusions [23–26]. Unigovski et al. showed that extruded alloys were more sensitive to the action of 3.5% NaCl solution in comparison with die-cast alloys [24]. This was attributed to the high plastic deformation of the former alloys, which led to strain hardening, an increased chemical potential of the metal and mechanochemical dissolution [27]. Nevertheless, the fatigue life of extruded alloys was significantly longer than that of die cast alloys [24]. Khan et al. reported little difference in the fatigue life of bare AM60 alloy and with a 1 μm thick anodic coating when tested under humid conditions; a 15 μm thick coating resulted in a poorer performance, which was ascribed to defects in the coating.

The present study investigates the effect of PEO on the fatigue behaviour of extruded AZ61 magnesium alloy in air of 33% relative humidity and in 3.5% NaCl aqueous solution. An alkaline

* Corresponding author. Tel.: +44 161 306 4872; fax: +44 161 206 4826.

E-mail address: p.skeldon@manchester.ac.uk (P. Skeldon).

silicate–pyrophosphate–fluoride electrolyte was chosen based on previous work [28]. In accordance with the findings of Khan et al. [22,23] on the influence of coating thickness on fatigue, a relatively thin coating, of $\sim 5 \mu\text{m}$ thickness, was chosen for the fatigue examination.

2. Materials and methods

2.1. Material and PEO treatment

AZ61 magnesium alloy was supplied by Magnesium Elektron Ltd. as extruded bars of 20 mm diameter. The chemical composition of the alloy is given in Table 1. Three types of specimen were employed for PEO: (i) flat specimens, cut transverse to the extrusion direction, of 20 mm diameter and 2.5 mm thickness for examination of the coating; (ii) fatigue specimens with a gauge section of length 15 mm and diameter 7 mm (see Fig. 1(a)); (iii) cylindrical specimens of length 50 mm and diameter 7 mm for assessment of the uniformity of coatings on a curved surface similar to that of the fatigue specimens. Specimens (ii) and (iii) were machined with their longitudinal axes in the extrusion direction. The flat surfaces of specimens (i) were ground to a 1200 grit finish using SiC paper and cleaned in acetone in an ultrasonic bath. The specimens were then gripped by steel clips to provide electrical connection and covered with lacquer 45 (MacDermid plc.), leaving a working area of $\sim 7 \text{ cm}^2$ [28]. Specimens (ii) and (iii) were mechanically polished to a 4000 grit finish using SiC papers. The cylindrical specimens were then gripped at one end by a steel clip and lacquer was applied to cover the clip and the end of the specimen, leaving an exposed length of 50 mm, with a working area of $\sim 11 \text{ cm}^2$. The fatigue specimens were similarly gripped and lacquered leaving the gauge length and shoulders exposed, with a working area of $\sim 11 \text{ cm}^2$.

PEO was carried out in 1 dm^{-3} of stirred electrolyte in a double-walled glass cell, with water cooling that maintained the electrolyte temperature in the range 293–303 K. The counter electrode was a cylinder of type 304 stainless steel, with a length of 150 mm and a diameter of 90 mm. The specimens were placed at the centre of the counter electrode. The coatings were formed at a constant root mean square (rms) current density of 130 mA cm^{-2} and a frequency 50 Hz, using a square waveform with a positive to negative current ratio of -1.2 . The electrolyte, which contained 10 g dm^{-3} sodium pyrophosphate ($\text{Na}_4\text{P}_2\text{O}_7 \cdot 10\text{H}_2\text{O}$), 11 g dm^{-3} sodium silicate solution (specific gravity 1.5), 2.5 g dm^{-3} potassium hydroxide (KOH) and 8 g dm^{-3} potassium fluoride (KF), was prepared using deionized water and analytical grade chemicals. The duration of the PEO treatment was 300 s. Following PEO, the specimens were rinsed with deionized water and dried in warm air. Fig. 1(b) shows the appearance of a fatigue specimen after PEO, with an off-white coating of uniform appearance on the gauge length.

2.2. Fatigue testing and specimen examination

The Young's modulus (E), yield strength (YS), ultimate tensile strength (UTS), elongation and reduction of area of the AZ61 alloy were determined using a TiraTest 2300 tensile test machine. The average values from three tensile tests are given in Table 2. High-cycle fatigue tests were carried out on the bare and

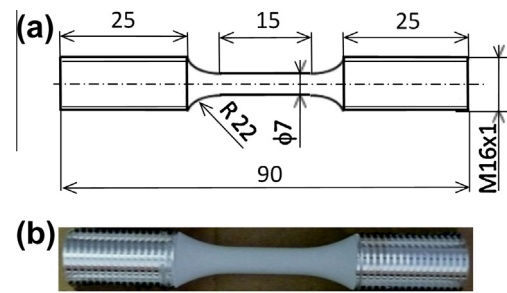


Fig. 1. (a) Schematic diagram of the fatigue specimen (dimensions in mm). (b) Photograph of a specimen after PEO for 300 s at 130 mA cm^{-2} (rms) in the silicate–pyrophosphate–fluoride electrolyte.

Table 2

Tensile properties of the AZ61 magnesium alloy.

E (GPa)	YS (MPa)	UTS (MPa)	Elongation (%)	Reduction of area (%)
43 ± 1.7	245 ± 2.2	329 ± 0.7	17.4 ± 0.7	30.8 ± 0.3

PEO-coated alloy using a PC controlled Amsler Vibrophore 422 machine, with a sinusoidal cycle of frequency 90 Hz, at room temperature in air of $33 \pm 5\%$ relative humidity and in 3.5% NaCl solution of pH 6.5. The ratio of the minimum stress to the maximum stress was 0. The solution was replenished during longer-term tests to maintain the pH within the range 6.5–7.2. For corrosion fatigue tests, a plastic cell containing naturally-aerated 0.5 dm^{-3} of 3.5% NaCl solution was attached to the specimens, which enabled the gauge length to be fully immersed in the solution. The fracture surfaces and gauge lengths of the specimens were examined using scanning electron microscopy (SEM), employing a Zeiss EVO50 instrument equipped with energy-dispersive X-ray (EDX) analysis facilities.

The adhesion/cohesion of the coating was evaluated by the scratch test method, using a Revetest system (CSM Instruments SA, Switzerland) equipped with a H-270 diamond indenter (200 μm diameter). Six scratch indentations were carried out under previously optimized conditions (linear progressive load mode 1–4 N, 4 N min^{-1}). In order to aid in determination of location of spallation/delamination, an extended scratch length of 6 mm was employed. The scratch tracks were subsequently observed by SEM to determine the locations of the first coating failure and to understand the nature of the coating failure. During the scratch tests, the loading force and penetration depth were recorded and their respective values were correlated with the observed failure locations. The surface roughness of the coating was evaluated using a surface roughness tester (TR200, Timegroup Inc.) according to ISO standard [29]. Due to the presence of the open porosity in the outer layer of the coating, a measurement length for determination of the roughness (R_a) of 0.8 mm was used. In total, eight measurements were carried out in different directions.

3. Results and discussion

3.1. PEO treatment

The surface of the coating formed following PEO treatment of a flat specimen for 300 s at 130 mA cm^{-2} is shown in the scanning electron micrograph of Fig. 2(a), which reveals a relatively uniform distribution of pores of size up to $\sim 5 \mu\text{m}$ and a network of fine cracks. Fig. 2(b) shows a cross-section of the specimen. The thickness of the PEO coating is $5.4 \pm 0.7 \mu\text{m}$. The alloy surface that was protected by lacquer during PEO can be seen at the left-hand side

Table 1

Chemical composition of the AZ61 magnesium alloy (wt%).

Al	Zn	Mn	Si	Fe	Ni	Cu	Others	Mg
6.20	0.61	0.22	0.02	0.001	0.0009	<0.001	<0.30	Bal.

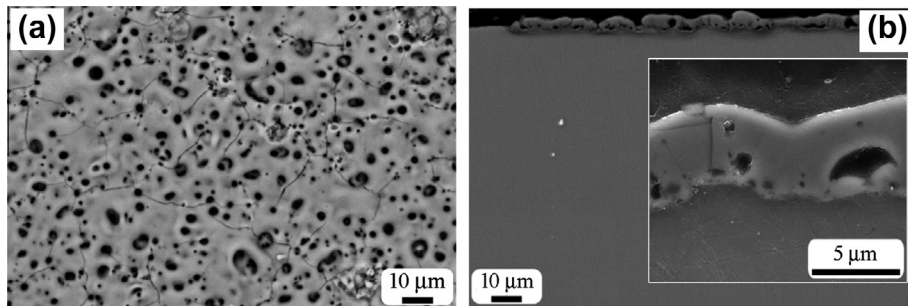


Fig. 2. Scanning electron micrographs (backscattered electrons) of a PEO coating formed on AZ61 magnesium alloy for 300 s at 130 mA cm^{-2} (rms) in the silicate–pyrophosphate–fluoride electrolyte; (a) surface and (b) cross-section.

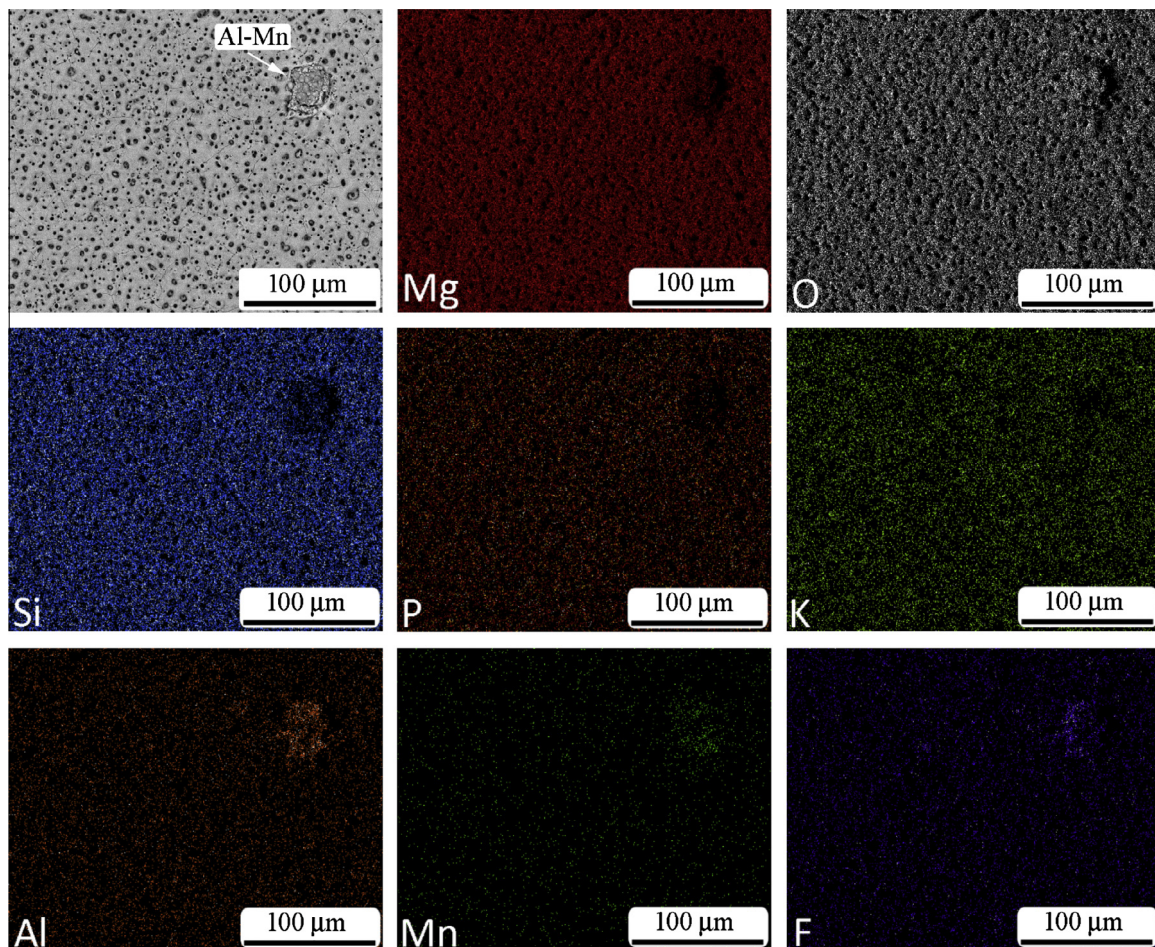


Fig. 3. EDX elemental mapping of the surface of AZ61 magnesium alloy with a PEO coating formed for 300 s at 130 mA cm^{-2} (rms) in the silicate–pyrophosphate–fluoride electrolyte.

of the micrograph. The outer half of the coating thickness lies above the original alloy surface. Thus, the growth of the coating has oxidized the alloy to a depth of $\sim 2.5 \mu\text{m}$. The inset image of Fig. 2(b) shows an enlargement of the coating, revealing a barrier layer next to the alloy, of roughly $1 \mu\text{m}$ thickness, an outer coating layer and an intermediate porous region of $\sim 1\text{--}2 \mu\text{m}$ thickness. From previous studies [28], EDX elemental mapping revealed a relatively uniform distribution of magnesium, fluorine, oxygen, phosphorus and silicon species throughout the coating thickness, with XRD indicating the presence of $\text{Mg}_3(\text{PO}_4)_2$ and possibly MgO . EDX mapping, shown in Fig. 3, discloses that Al–Mn second phase

particles in the alloy modified the local composition and morphology of the coating, with the concentration of fluorine increased and that of magnesium, silicon, phosphorus and potassium decreased near the particles.

The surface roughness of the coating was determined as $2.4 \pm 0.5 \mu\text{m}$. The measurement of roughness was made over regions that excluded the large open pores, which can penetrate deeply into the outer layer. No effect of the measurement direction was observed, indicating that the coating surface does not have any direction-related texture. A detailed study of the porosity of PEO coatings has indicated a wide range of pore size, including fine

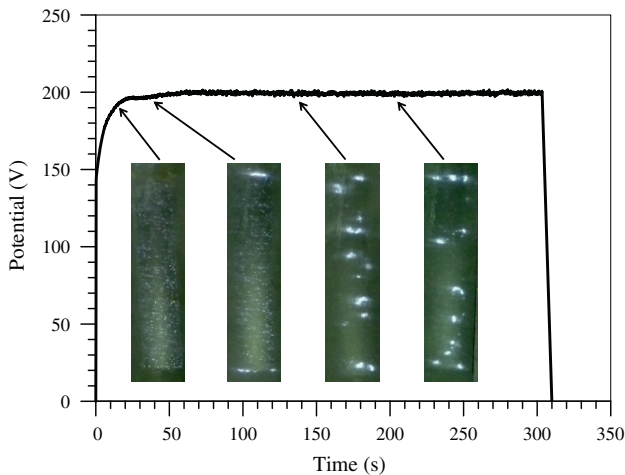


Fig. 4. Voltage–time response and appearance of sparks during PEO of a cylindrical specimen of AZ61 magnesium alloy for 300 s at 130 mA cm^{-2} (rms) in the silicate–pyrophosphate–fluoride electrolyte.

pores of $\sim 5 \text{ nm}$ diameter that are not resolved by conventional SEM [30]. A surface-connected porosity of 20% was estimated, with negligible occluded porosity.

Fig. 4 shows the voltage–time response and the appearance of a cylindrical specimen during PEO. The voltage rose to $\sim 190 \text{ V}$ in 25 s, when small, white discharges appeared. It then increased slowly to $\sim 200 \text{ V}$ after 60 s, with large, white discharges becoming evident, first at the specimen edges and then elsewhere. Scanning electron micrographs of cross-sections of the cylindrical specimen at distances of 10, 25 and 40 mm from the bottom end are shown in Fig. 5. There were no significant differences in the coatings at the three locations, which were of thicknesses 5.2 ± 0.7 , 5.8 ± 0.9 and $6.4 \pm 0.8 \mu\text{m}$ at the respective positions. The thicknesses are similar to that of the flat specimen, namely $5.4 \pm 0.7 \mu\text{m}$, which produced a similar voltage–time response to that of Fig. 4.

3.2. Adhesion/cohesion of the coating

Scratch testing indicated that the coating failure mode was of a cohesive nature and that the initial micro-cracking developed at the interface between the outer and inner layers of the coating. Spallation and subsequent delamination of the outer layer was recorded under a load of $2.69 \pm 0.10 \text{ N}$, which corresponds to a track length of approximately $3.4 \pm 0.2 \text{ mm}$ from the scratch start point. The lower layer of the coating did not detach from the substrate, as

shown in Fig. 6. Instead, the layer was pushed deeper into the magnesium substrate, which was confirmed by SEM observations; no substrate could be observed in the track even at penetration depths of $31.5 \pm 9.7 \mu\text{m}$, which was the average of the depths recorded at the end of the scratch tracks. The failure mode observed is in agreement with the scratch testing model of a hard coating–soft substrate given by Bull and Berasetegui [31] and indicates that the cohesive strength of the coating layers is less than the adhesive strength between the coating and the substrate.

3.3. Fatigue tests

The results of fatigue tests are shown in Fig. 7. The tests that reached 10^7 cycles, marked with arrows, were terminated before fracture of the specimens. The data were fitted by minimizing the sum of squares of the deviations with two regression functions [32]:

$$\text{Kohout and Věchet : } \sigma(N) = \sigma_{\infty} \left(\frac{N_f}{N_f + C} \right)^b, \quad (1)$$

$$\text{Stromeyer : } \sigma(N) = a \cdot N_f^b + \sigma_{\infty}, \quad (2)$$

where a , b , C and σ_{∞} are parameters of the regression function, N_f is the number of cycles and σ is the maximum applied stress measured in MPa. The K and V function gave a better fit to data above 10^5 cycles, as shown for the uncoated specimen tested in air, and only this fitting is shown for other test conditions. Fig. 7 reveals the highest fatigue strength for the bare alloy tested in air and the lowest fatigue strength for the coated alloy tested in 3.5% NaCl solution. The bare alloy exposed to 3.5% NaCl and the coated alloy exposed to air exhibited similar, intermediate fatigue behaviours. The fatigue strengths predicted at 10^7 cycles are listed in Table 3 together with the parameters of the K and V function. For aluminium or magnesium alloys, which have no well-defined fatigue limit, it is common to report the fatigue strength at 10^8 cycles. However, the present fitted curves suggested that the fatigue strengths at 10^7 and 10^8 cycles differ by less than 2%. The fatigue limit of the bare alloy in air and 3.5% NaCl solution was 145.4 and 88.0 MPa respectively, indicating a reduction of 40% due to the NaCl solution. The corresponding values for the PEO-coated alloy were 91.5 and 63.8 MPa, indicating reductions of $\sim 40\%$ and 56% in comparison with the bare alloy in air. Bhuiyan et al. [25] found an 85% reduction of the fatigue limit of bare AZ61 alloy in 5% NaCl solution, which exceeds the present reduction of 40%. However, Yerokhin et al., for a different magnesium alloy and PEO process, reported reductions of up to 10% for tests in air, compared with 40% for the present coating [21].

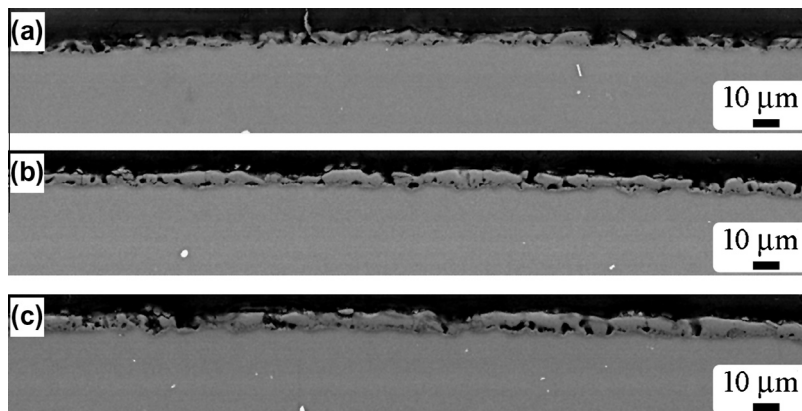


Fig. 5. Cross-sections of a cylindrical specimen of AZ61 magnesium alloy at distances of (a) 10 mm, (b) 25 mm and (c) 40 mm measured from the bottom end following PEO for 300 s at 130 mA cm^{-2} (rms) in the silicate–pyrophosphate–fluoride electrolyte.

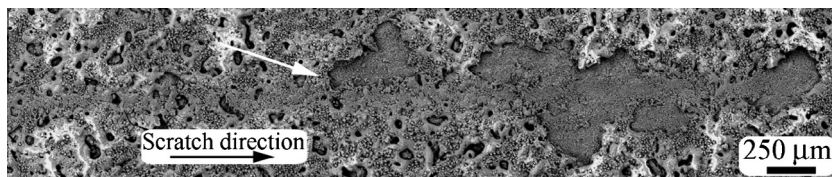


Fig. 6. Scanning electron micrograph of the scratch test track. The arrow indicates the first occurrence of outer layer delamination; no substrate was visible following detachment of the outer layer.

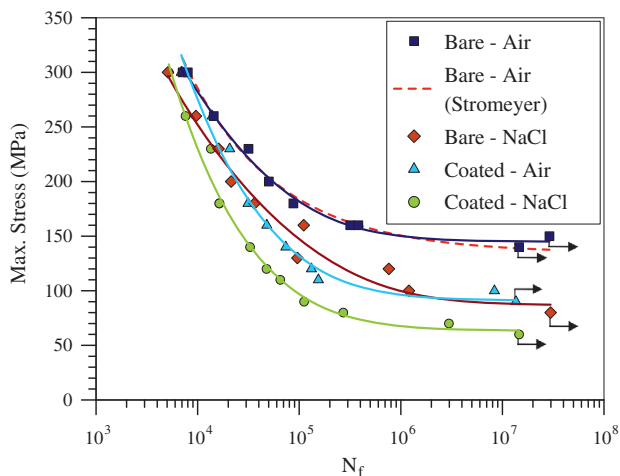


Fig. 7. S–N curves of extruded AZ61 magnesium alloy in the bare and coated conditions tested in air and 3.5% NaCl solution fitted with the Kohout and Věchet function. A fit using the Stromeyer function is also shown for the bare alloy tested in air.

Table 3

Parameters of Kohout and Věchet function determined by fitting experimental data and predicted fatigue limits at 10^7 cycles.

Alloy/environment	Parameters			σ_c for 10^7 cycles	
	b	C	σ_∞ (MPa)	(MPa)	
Bare-air	–0.234	163540.8	144.9	145.4	
Bare-NaCl	–0.245	769659.9	86.7	88.0	
Coated-air	–0.394	155577.2	99.0	91.5	
Coated-NaCl	–0.466	148936.1	63.4	63.8	

3.4. Fractographic analysis

Three specimens, from the start, middle and end of the each S–N curve respectively, were chosen for fractographic analysis. The fracture surfaces of the specimens are shown in the low magnification scanning electron micrographs of Fig. 8, which reveal an increase in the region of fatigue with decrease of the stress amplitude. Coated specimens tested in air at the two highest stresses had a greater number of crack initiation sites than the bare alloy. Several initiation sites also occurred on the bare and coated alloy in 3.5% NaCl solution at the highest stress amplitude. At relatively low stress amplitudes, only one initiation site was evident on both bare and coated specimens tested in either air or NaCl solution.

Crack initiation in the bare alloy tested in air often occurred near Al–Mn particles, which were typically of size between 1 and 15 μm . The backscattered electron micrographs of Fig. 9(a and b) shows examples for a test in air under stress amplitudes of 200 and 300 MPa, in which the particles are evident on the main fatigue crack (Fig. 9(a)) and at secondary cracks on the gauge length (Fig. 9(b)). The crack initiation is probably related to the stress

enhancement that results from the large difference in hardness between the particles and the matrix [33–35]. The hardness of the particles has been determined previously as 948 ± 61 HV, compared with 64 ± 2 HV_{0.1} for the matrix [28].

In the presence of the 3.5% NaCl solution, fatigue cracks initiated at regions of localized corrosion of the alloy, as shown by the example of Fig. 9(c and d) for a test at a stress amplitude of 120 MPa. EDX analysis at these locations revealed 60 at.% O, 26 at.% Mg, 7 at.% Al, 1 at.% Si and 6 at.% Cl, with the presence of oxygen and chlorine being associated with corrosion products. Other studies [23,24,26,36] have shown also that corrosion sites are favourable for fatigue crack initiation. Localized corrosion is promoted by corrosion cells formed by second phase particles and the matrix, which cause dissolution of the matrix adjacent to the particles [8]. Further, Bhuiyan et al. showed that cyclic loading of AZ80 alloy can enhance localized corrosion compared with the non-stressed condition [37]. The number of secondary cracks on the gauge length reduced with reducing stress amplitude for tests of the bare alloy both in air and in NaCl solution. At high stress amplitude, relatively large secondary cracks occurred over most of the gauge length whereas, under a low stress, such cracks were finer and confined mainly to the vicinity of the fracture surface.

For tests both in air and 3.5% NaCl solution, the fatigue crack surface had a coarse lamellar appearance near the initiation site, with secondary cracks that propagated along the lamellae, as revealed in Fig. 10(a) for a test in air at a stress amplitude of 160 MPa. Paired features, indicated by arrows in Fig. 10(b), on the fracture surface generated in NaCl solution, are possibly indications of twin boundaries [36]. The fracture surface close to the final fracture was of smoother appearance (Fig. 10(c)), as observed in other work [36]. Secondary cracks and striations, the latter indicated by arrows, were observed in this area (Fig. 10(d)).

Cross-sections of specimens were examined for tests carried out at a stress amplitude of 160 MPa in air and in 3.5% NaCl solution. Fig. 11(a) shows twins adjacent to the fatigue crack generated in 3.5% NaCl solution. The twins were particularly apparent from a depth of about 30% of the specimen diameter and were most abundant near the end of fatigue crack. Similar twinning was observed in the specimen tested in air. The occurrence of twinning in the region of fatigue crack propagation agrees with previous work [38,39]. Other studies have considered in detail the occurrence of twinning during fatigue testing. Zeng et al. found that crack initiation and propagation in extruded AM60 is related to the synergistic influences of slip bands, double twinning, intermetallic compounds and grain boundaries [35]. Shiozawa et al. observed crack growth along twin boundaries in an extruded AZ80Mg alloy, with the direction of propagation changing at grain boundaries [40]. Zhang et al. examined the formation of twins ahead of the crack tip during cyclic deformation of an extruded AZ61A alloy under different loading modes, finding the highest volume fraction of the residual twins under tension–compression, with almost every grain containing twins on reaching a strain amplitude of 1% [41].

The cross-section of Fig. 11(a) reveals that the alloy had a duplex grain size, with a non-uniform distribution of large grains, up to ~ 40 μm size, and fine grains, ~ 1 μm in size. This hindered

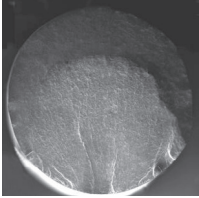
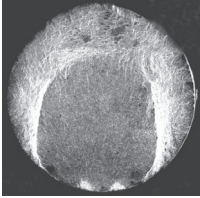
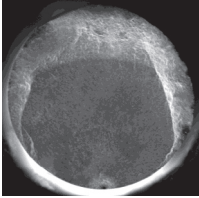
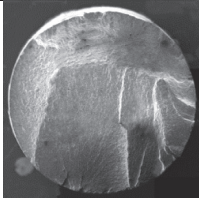
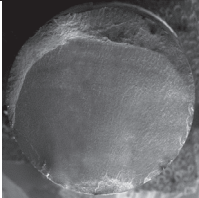
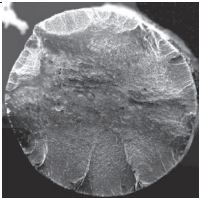
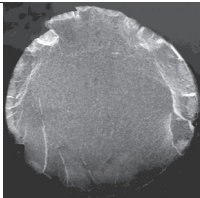
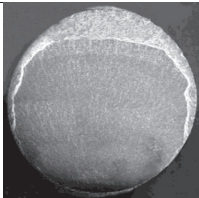
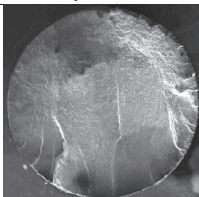
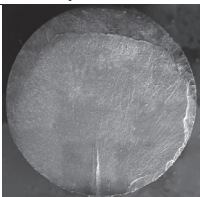
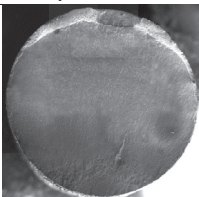
	High stress	Medium stress	Low stress
Bare Air	 $\sigma_{\max} = 260 \text{ MPa}$, $N_f = 14400$	 $\sigma_{\max} = 200 \text{ MPa}$, $N_f = 50200$	 $\sigma_{\max} = 160 \text{ MPa}$, $N_f = 381800$
Bare NaCl	 $\sigma_{\max} = 260 \text{ MPa}$, $N_f = 9600$	 $\sigma_{\max} = 160 \text{ MPa}$, $N_f = 110800$	 $\sigma_{\max} = 120 \text{ MPa}$, $N_f = 763000$
Coated Air	 $\sigma_{\max} = 300 \text{ MPa}$, $N_f = 6900$	 $\sigma_{\max} = 160 \text{ MPa}$, $N_f = 48000$	 $\sigma_{\max} = 100 \text{ MPa}$, $N_f = 8345100$
Coated NaCl	 $\sigma_{\max} = 230 \text{ MPa}$, $N_f = 13500$	 $\sigma_{\max} = 120 \text{ MPa}$, $N_f = 47600$	 $\sigma_{\max} = 70 \text{ MPa}$, $N_f = 2975900$

Fig. 8. Scanning electron micrographs of the fracture surfaces of AZ61 magnesium alloy without and with PEO coating tested in air and in 3.5% NaCl solution.

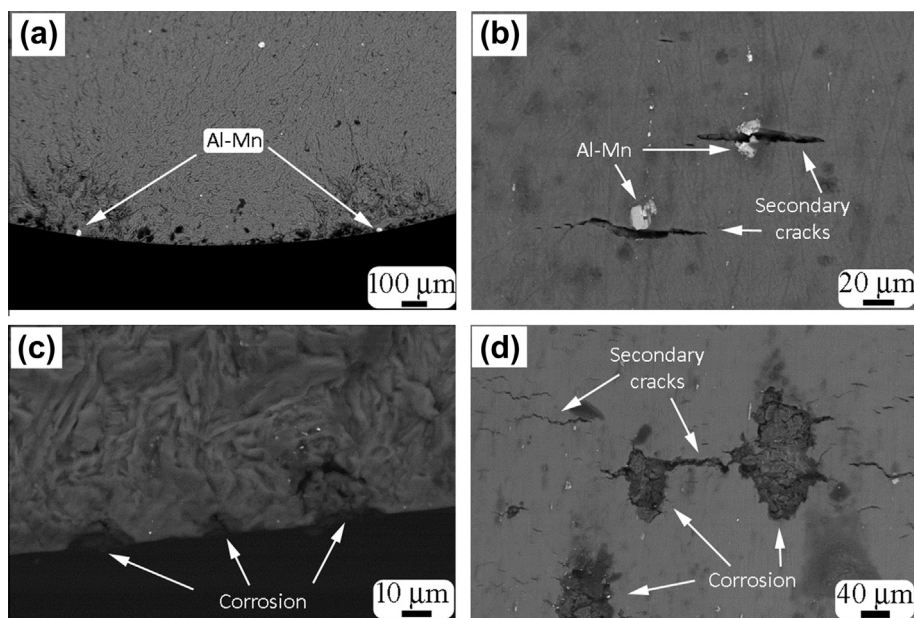


Fig. 9. Scanning electron micrographs showing fatigue crack initiation in the bare AZ61 magnesium alloy: (a) air – fracture surface, $\sigma_{\max} = 200 \text{ MPa}$, $N_f = 50,200$; (b) air – gauge length close to the fracture, $\sigma_{\max} = 300 \text{ MPa}$, $N_f = 7100$; (c) 3.5% NaCl solution – fracture surface, $\sigma_{\max} = 160 \text{ MPa}$, $N_f = 110,800$; (d) 3.5% NaCl solution – gauge length close to the fracture, $\sigma_{\max} = 120 \text{ MPa}$, $N_f = 763,000$.

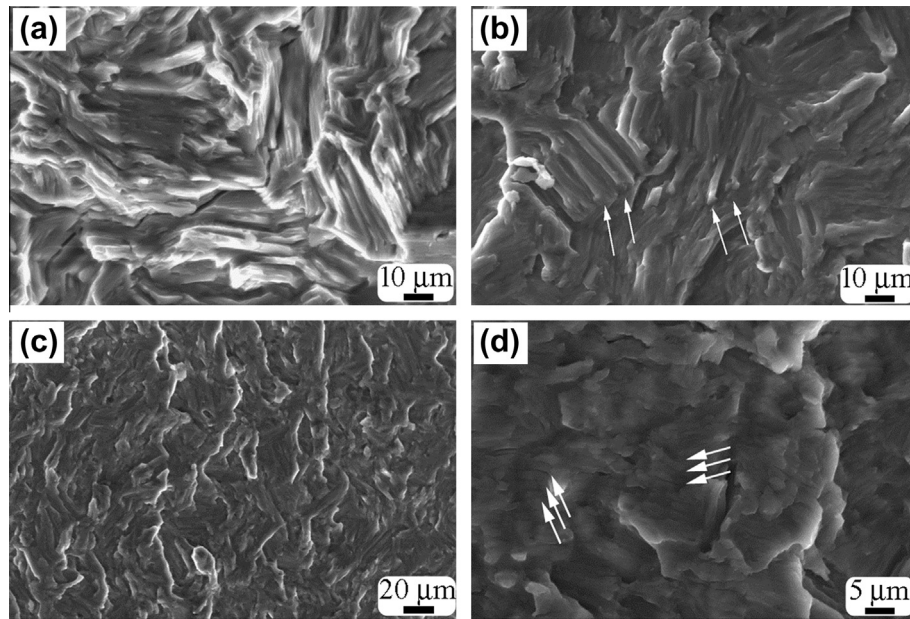


Fig. 10. Scanning electron micrographs of the fatigue crack propagation region of bare AZ61 magnesium alloy tested in (a) air, $\sigma_{\max} = 160$ MPa, $N_f = 381,800$; (b) 3.5% NaCl solution, $\sigma_{\max} = 160$ MPa, $N_f = 110,800$; (c) 3.5% NaCl solution, $\sigma_{\max} = 120$ MPa, $N_f = 763,000$; (d) PEO-coated alloy tested in 3.5% NaCl solution, $\sigma_{\max} = 230$ MPa, $N_f = 13,500$.

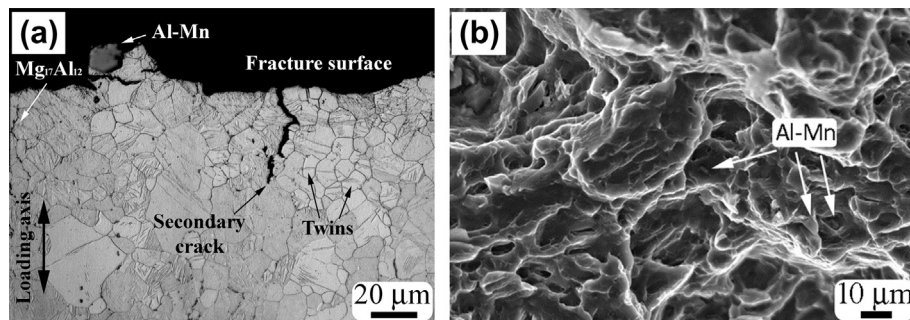


Fig. 11. (a) Optical micrograph showing twins beneath the fatigue fracture of bare AZ61 magnesium alloy tested in 3.5% NaCl solution, $\sigma_{\max} = 160$ MPa, $N_f = 110,800$. (b) Scanning electron micrograph of the final fracture in air of PEO-coated AZ61 magnesium alloy, $\sigma_{\max} = 300$ MPa, $N = 6900$.

identification of the crack path, which appeared to be mainly transgranular, although the presence of intergranular regions could not be ruled out. The cross-section displays secondary cracks and decohesion of Al–Mn particles, as well as $Mg_{17}Al_{12}$ at grain boundaries. The final fracture surfaces in all test conditions revealed a dimpled appearance, characteristic of a ductile failure. Al–Mn particles were observed inside the dimples. A representative example of the final fracture is shown for a coated specimen tested in air at a stress amplitude of 300 MPa (Fig. 11(b)).

In the case of tests of the coated alloy, spalling of the outer layer of the coating was observed. The spalling was confined to the region of the gauge length near the main fracture under low or medium stress amplitudes. In contrast, under a high stress amplitude, spalling of the outer layer affected most of the gauge length. An example of the spalling is provided by the photograph of a specimen tested at 180 MPa shown in the inset of Fig. 12(a), which reveals a slightly darker, adherent inner layer where the outer coating layer has detached. Fig. 12(a) also shows a micrograph of the boundary of the spalled region, which discloses narrow cracks, transverse to the loading axis, in the outer coating layer and occasional fine cracks in the inner layer.

Fig. 12(b) shows a relatively rough fracture surface near a site of fatigue crack initiation, with a transition to a region of a smoother

appearance, in a coated specimen tested in air at a low stress amplitude of 100 MPa, similar to observations for the bare alloy. Fatigue cracks on a specimen tested in NaCl solution at a low stress amplitude of 70 MPa appeared to initiate at a few closely-spaced sites, where beach-mark-like features were observed, as shown in Fig. 13(a). At low stress amplitudes, secondary cracking of the alloy on the gauge length was negligible, although a network of fine cracks in the coating was evident. In contrast, secondary cracks were relatively abundant at higher stress levels. Fig. 13(b) shows a secondary crack near an Al–Mn particle on the gauge length of a coated specimen tested in NaCl solution at a relatively high stress amplitude of 300 MPa. Under low stress amplitudes, a layer of corrosion product formed beneath the coating; Fig. 14 shows a specimen tested at 60 MPa for a time of ~ 45 h, which displays a ~ 2 μm thick layer. The corrosive environment can reach the substrate through the open pores and cracks formed due to either the PEO process or the cyclic loading. Liang et al. [42] has previously suggested that the formation of magnesium hydroxide at the alloy/coating interface exerts a stress that can lift the coating from the substrate.

The degradation of fatigue properties of the AZ61 alloy after PEO treatment is probably due to a combination of factors, including stress concentration, that results from cracks in the coating layer [22], the roughness of the alloy/coating interface [22], and

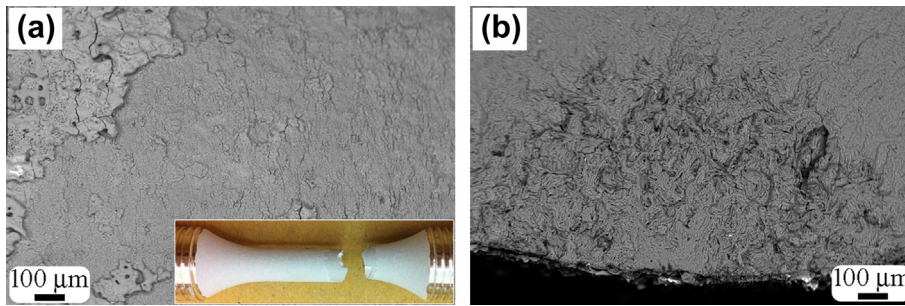


Fig. 12. (a) Scanning electron micrographs showing spalling of the outer coating layer from the gauge length of PEO-coated AZ61 magnesium alloy tested in air, $\sigma_{\max} = 180$ MPa, $N_f = 31,300$. (Inset: photograph of the specimen.) (b) Fatigue crack initiation in the PEO-coated alloy tested in air, $\sigma_{\max} = 100$ MPa, $N_f = 8,345,100$.

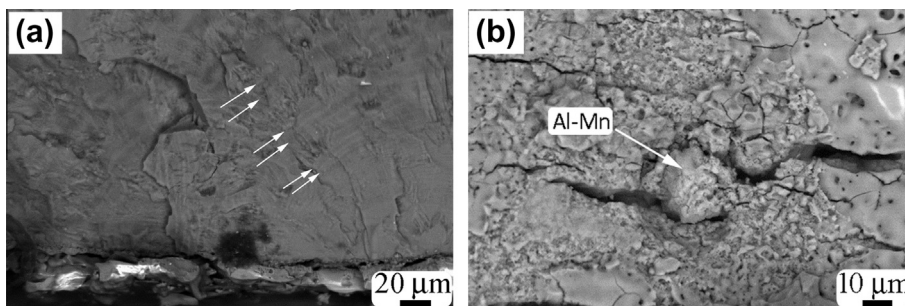


Fig. 13. Scanning electron micrographs of fatigue crack initiation in the PEO-coated AZ61 magnesium alloy tested in 3.5% NaCl solution: (a) fracture surface with beach-mark-like features (marked with arrows), $\sigma_{\max} = 70$ MPa, $N_f = 2,975,900$; (b) gauge length close to the fracture surface, $\sigma_{\max} = 300$ MPa, $N_f = 5200$.

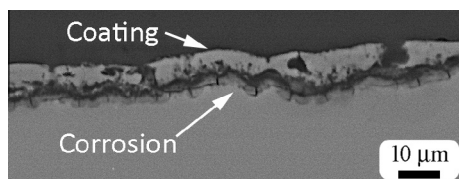


Fig. 14. Scanning electron micrograph showing corrosion of PEO-coated AZ61 magnesium alloy tested in 3.5% NaCl solution; $\sigma_{\max} = 60$ MPa, $N = 14,588,900$, test stopped without fracture of the specimen.

corrosion beneath the coating, which enhance the stress locally in the alloy surface and assist crack initiation, leading to the higher number of initiation sites observed on the coated specimens compared with the bare alloy. Bhuiyan et al. [43] also considered that cracks developed during loading affect the residual stresses in the coating, which were assumed to be compressive, as measured in PEO coatings on aluminium alloys [44–46]. Lonyuk et al. indicated that compressive residual stresses in the coating retard fatigue crack initiation and therefore increase the fatigue life [46]. However, if the compressive residual stress is high, coating delamination and cracking may occur. They also found that cracks initiated in the substrate adjacent to the coating, mainly at locations where the coating was thicker.

4. Conclusions

1. PEO treatment of AZ61 magnesium alloy in the silicate–pyrophosphate–fluoride electrolyte, forming a $\sim 5\text{--}6$ μm thick coating, resulted in a reduction of the high-cycle fatigue limit in air from 145.4 MPa to 91.5 MPa, and a further reduction to 63.8 MPa in 3.5% NaCl solution. Experimental fatigue data could be best fitted by the Kohout and Věchet regression.
2. Fatigue cracks in the uncoated alloy tested in air initiated mainly at Al–Mn particles. The presence of sodium chloride

solution caused corrosion of the alloy matrix around Al–Mn particles and the formation of corrosion pits, leading to stress concentration and fatigue crack initiation.

3. PEO enhanced stresses in the alloy surface, due to the roughness of the alloy/coating interface and stress transfer following cracking of the coating, which resulted in multiple crack initiation sites. Cyclic loading caused the outer coating layer to spall over an area of the gauge length that increased with the stress amplitude. In the presence of 3.5% NaCl solution, cracks and pores in the coating allowed the solution to reach the alloy, with corrosion then spreading under the coating leading to further degradation of the fatigue performance.
4. The fatigue crack propagation area had similar characteristic in all tested conditions, i.e. a coarse appearance with secondary cracks in the area close to initiation and a finer appearance in the area close to final fracture. Secondary cracks also occurred in the region of fatigue crack propagation. Dimples, containing Al–Mn particles, characterized the overload fracture.

Acknowledgements

The authors are grateful to the Engineering and Physical Sciences Research Council (U.K.) (Programme Grant: LATEST2) and the European Regional Development Fund, in the framework of the research project NETME Centre under the Operational Programme Research and Development for Innovation, for support of the work.

References

- [1] B.L. Mordike, T. Ebert, *Magnesium – properties – application – potential*, Mater. Sci. Eng. A 302 (2001) 37–45.
- [2] K.U. Kainer, *Magnesium Alloys and Technology*, WILEY-VCH, Weinheim, 2003.
- [3] E. Ghali, *Corrosion Resistance of Aluminium and Magnesium Alloys, Understanding, Performance and Testing*, Wiley, United States, 2010.

- [4] K.U. Kainer, B.S. Bala, C. Blawert, W. Dietzel, Shreifs Corrosion, vol. 3, Elsevier, UK, 2010 (Chapter 9).
- [5] Y. Song, E. Han, D. Shan, C.D. Yim, B.S. You, The role of second phases in the corrosion behaviour of Mg–5Zn alloy, *Corros. Sci.* 60 (2012) 238–245.
- [6] J.D. Majumdera, R. Galun, B.L. Mordike, I. Manna, Effect of laser surface melting on corrosion and wear resistance of a commercial magnesium alloy, *Mater. Sci. Eng. A* 361 (2003) 119–129.
- [7] G. Song, A. Atrens, Corrosion mechanisms of magnesium alloys, *Adv. Eng. Mater.* 1 (1999) 11–33.
- [8] R. Zeng, J. Zhang, W. Huang, W. Dietzel, K.U. Kainer, C. Blawert, K.E. Wei, Review of studies on corrosion of magnesium alloys, *Trans. Nonferrous Met. Soc. China* 16 (2006) 763–771.
- [9] M. Liu, P.J. Uggowitzer, A.V. Nagasekhar, P. Schmutz, M. Easton, G. Song, A. Atrens, Calculated phase diagrams and the corrosion of die-cast Mg–Al alloys, *Corros. Sci.* 51 (2009) 602–619.
- [10] J. Sudagar, J. Lian, X. Chen, P. Lang, Y. Liang, High corrosion resistance of electroless Ni–P with chromium-free conversion pre-treatments on AZ91D magnesium alloy, *Trans. Nonferrous Met. Soc. China* 21 (2011) 921–928.
- [11] C.E. Barchiche, D. Veys-Renaux, E. Rocca, A better understanding of PEO on Mg alloys by using a simple galvanostatic electrical regime in a KOH–KF–Na₃PO₄ electrolyte, *Surf. Coat. Technol.* 205 (2011) 4243–4248.
- [12] E. Matykina, R. Arrabal, P. Skeldon, G.E. Thompson, P. Belonguer, AC PEO of aluminium with porous alumina precursor films, *Surf. Coat. Technol.* 205 (2010) 1668–1678.
- [13] F. Chen, H. Zhou, B. Yao, Z. Qin, Q. Zhang, Corrosion resistance property of the ceramic coating obtained through microarc oxidation on the AZ31 magnesium alloy surfaces, *Surf. Coat. Technol.* 201 (2007) 4905–4908.
- [14] A.L. Yerokhin, X. Nie, A. Leyland, A. Matthews, S.J. Dowey, Plasma electrolysis for surface engineering, *Surf. Coat. Technol.* 122 (1999) 73–93.
- [15] R. Arrabal, A. Pardo, M.C. Merino, M. Moledano, P. Casajús, E. Matykina, P. Skeldon, G.E. Thompson, Corrosion behaviour of a magnesium matrix composite with silicate plasma electrolytic oxidation coating, *Corros. Sci.* 52 (2010) 3738–3749.
- [16] H. Duan, C. Yan, F. Wang, Effect of electrolyte additives on performance of plasma electrolytic oxidation films formed on magnesium alloy AZ91D, *Electrochim. Acta* 52 (2007) 3785–3793.
- [17] L. Wang, L. Chen, Z. Yan, H. Wang, J. Peng, Effect of potassium fluoride on structure and corrosion resistance of plasma electrolytic oxidation films formed on AZ31 magnesium alloy, *J. Alloys Compd.* 480 (2009) 469–474.
- [18] H.A. Prescott, L. Zhi-Jian, E. Kemnitz, J. Deutschb, H. Lieske, New magnesium oxide fluorides with hydroxy groups as catalysts for Michael additions, *J. Mater. Chem.* 15 (2005) 4616–4628.
- [19] J. Liang, B. Guo, J. Tian, H. Liu, J. Zhou, T. Xu, Effect of potassium fluoride in electrolytic solution on the structure and properties of microarc oxidation coatings on magnesium alloy, *Appl. Surf. Sci.* 252 (2005) 345–351.
- [20] J.E. Gray, B. Luan, Protective coatings on magnesium and its alloys – a critical review, *J. Alloys Compd.* 336 (2002) 88–113.
- [21] A.L. Yerokhin, A. Shatrov, V. Samsonov, P. Shashkov, A. Leyland, A. Matthews, Fatigue properties of Keronite coatings on a magnesium alloy, *Surf. Coat. Technol.* 182 (2004) 78–84.
- [22] S.A. Khan, Y. Miyashita, Y. Mutoh, T. Koike, Effect of anodized layer thickness on fatigue behaviour of magnesium alloy, *Mater. Sci. Eng. A* 474 (2008) 261–269.
- [23] S.A. Khan, Y. Miyashita, Y. Mutoh, T. Koike, Fatigue behaviour of anodized AM60 magnesium alloy under humid environment, *Mater. Sci. Eng. A* 498 (2008) 377–383.
- [24] Y. Unigovski, A. Eliezer, E. Abramov, Y. Snir, E.M. Gutman, Corrosion fatigue of extruded magnesium alloys, *Mater. Sci. Eng. A* 360 (2003) 132–139.
- [25] M.S. Bhuiyan, Y. Mutoh, T. Murai, S. Iwakami, Corrosion fatigue behaviour of extruded magnesium alloy AZ61 under three different corrosive environments, *Int. J. Fatigue* 30 (2008) 1756–1765.
- [26] Z.B. Sajuri, Y. Miyashita, Y. Mutoh, Effects of humidity and temperature on the fatigue behaviour of an extruded AZ61 magnesium alloy, *Fatigue Fract. Eng. M* 28 (2005) 373–379.
- [27] E.M. Gutman, A. Eliezer, Y. Unigovski, E. Abramov, Mechano-electrochemical behaviour and creep corrosion of magnesium alloys, *Mater. Sci. Eng. A* 302 (2001) 63–67.
- [28] A. Němcová, P. Skeldon, G.E. Thompson, B. Pacal, Effect of fluoride on plasma electrolytic oxidation of AZ61 magnesium alloy, *Surf. Coat. Technol.* 232 (2013) 827–838.
- [29] ISO 4287-1997: Geometrical Product Specifications (GPS) – Surface texture: Profile method – Terms, definitions and surface texture parameters, International Organization for Standardization.
- [30] J.A. Curran, T.W. Clyne, Porosity in plasma electrolytic coatings, *Acta Mater.* 54 (2006) 1985–1993.
- [31] S.J. Bull, E.G. Berasetegui, An overview of the potential of quantitative coating adhesion measurement by scratch testing, *Tribol. Int.* 39 (2006) 99–114.
- [32] J. Kohout, S. Věchet, A new function for fatigue curves characterization and its multiple merits, *Int. J. Fatigue* 23 (2001) 175–183.
- [33] M. Horynová, J. Zapletal, P. Doležal, P. Gejdoš, Evaluation of fatigue life of AZ31 magnesium alloy fabricated by squeeze casting, *Mater. Des.* 45 (2013) 253–264.
- [34] S.A. Khan, Y. Miyashita, Y. Mutoh, Z.B. Sajuri, Influence of Mn content on mechanical properties and fatigue behaviour of extruded Mg alloys, *Mater. Sci. Eng. A* 420 (2006) 315–321.
- [35] R. Zeng, E. Han, W. Ke, W. Dietzel, K.U. Kainer, A. Atrens, Influence of microstructure on tensile properties and fatigue crack growth in extruded magnesium alloy, AM60, *Int. J. Fatigue* 32 (2010) 411–419.
- [36] A.N. Chamos, Sp.G. Pantelakis, V. Spiladis, Fatigue behaviour of bare and pre-corroded magnesium alloy AZ31, *Mater. Des.* 31 (2010) 4130–4137.
- [37] M.S. Bhuiyan, Y. Mutoh, T. Murai, S. Iwakami, Corrosion fatigue behaviour of extruded magnesium alloy AZ80–T5 in a 5% NaCl environment, *Eng. Fract. Mech.* 77 (2010) 1567–1576.
- [38] Q. Yu, J. Zhang, Y. Jiang, Q. Li, Effect of strain ratio on cyclic deformation and fatigue of extruded AZ61A magnesium alloy, *Int. J. Fatigue* 44 (2012) 225–233.
- [39] S.M. Yin, F. Yang, X.M. Yang, S.D. Wu, S.X. Li, G.Y. Li, The role of twinning-detwinning on fatigue fracture morphology of Mg–3%Al–1%Zn alloy, *Mater. Sci. Eng. A* 494 (2008) 397–400.
- [40] K. Shiozawa, T. Kashiwagi, T. Murai, T. Takahashi, Fatigue behaviour and fractography of extruded AZ80 magnesium alloys in very high cycle regime, *Procedia Eng.* 2 (2010) 183–191.
- [41] J. Zhang, Q. Yu, Y. Jiang, Q. Li, An experimental study of cyclic deformation of extruded AZ61A magnesium alloy, *Int. J. Plasticity* 27 (2011) 768–787.
- [42] J. Liang, P.B. Srinivasan, C. Blawert, M. Störmer, W. Dietzel, Electrochemical corrosion behaviour of plasma electrolytic oxidation coatings on AM50 magnesium alloy formed in silicate and phosphate based electrolytes, *Electrochim. Acta* 54 (2009) 3842–3850.
- [43] M.S. Bhuiyan, Y. Ostuka, Y. Mutoh, T. Murai, S. Iwakami, Corrosion fatigue of conversion coated AZ61 magnesium alloy, *Mater. Sci. Eng. A* 527 (2010) 4978–4984.
- [44] R.H.U. Khan, A.L. Yerokhin, T. Pilkington, A. Leyland, A. Matthews, Residual stresses in plasma electrolytic oxidation coatings on Al alloy produced by pulsed unipolar current, *Surf. Coat. Technol.* 200 (2005) 1580–1586.
- [45] D.T. Asquith, A.L. Yerokhin, J.R. Yates, A. Matthews, Effect of combined shot-peening and PEO treatment on fatigue life of 2024 Al alloy, *Thin Solid Films* 515 (2006) 1187–1191.
- [46] B. Lonyuk, I. Apachitei, J. Duszczuk, The effect of oxide coatings on fatigue properties of 7475-T6 aluminium alloy, *Surf. Coat. Technol.* 201 (2007) 8688–8694.